Analytical Modeling and Multiphysics Simulation of Acousto-Electromagnetic Interaction

Wingren, Niklas; Sjoberg, Daniel

Published in:
14th European Conference on Antennas and Propagation, EuCAP 2020

DOI:
10.23919/EuCAP48036.2020.9135567

2020

Document Version:
Peer reviewed version (aka post-print)

Link to publication

Citation for published version (APA):
Wingren, N., & Sjoberg, D. (2020). Analytical Modeling and Multiphysics Simulation of Acousto-Electromagnetic Interaction. In *14th European Conference on Antennas and Propagation, EuCAP 2020* Article 9135567 (14th European Conference on Antennas and Propagation, EuCAP 2020). IEEE - Institute of Electrical and Electronics Engineers Inc.. https://doi.org/10.23919/EuCAP48036.2020.9135567

Total number of authors:
2

LUND UNIVERSITY

PO Box 117
221 00 Lund
+46 46-222 00 00

Analytical Modeling and Multiphysics Simulation of Acousto-Electromagnetic Interaction

Niklas Wingren*, Daniel Sjöberg*
*Department of Electrical and Information Technology, Lund University, Lund, Sweden, niklas.wingren@eit.lth.se

***Abstract*—A model for interaction between acoustic and electromagnetic waves based on photoelasticity is presented. A radar equation based on physical, geometric and system parameters is shown, as well as a condition for maximizing interaction (equivalent to the Bragg condition in acousto-optics). The photoelastic model is used to implement a multiphysics simulation of the problem. The Bragg condition is shown to hold for the simulated case. Additionally, simulations are used to show how a contrast in material properties in a small inclusion affects the interaction.**

***Index Terms*—multiphysics, photoelasticity, electromagnetic scattering, acoustics.**

I. INTRODUCTION

Interaction between acoustic and electromagnetic waves has been studied since at least 1922 when Brillouin described what would later be known as acousto-optics [1]. The connection between these seemingly separate phenomena occurs as an acoustic wave can affect its medium in various ways, altering conditions for electromagnetic waves in the region.

A well-established interaction mechanism is in acousto-optics, where interaction is based on ultrasound modulating the refractive index [2]. An optical beam is then diffracted by this modulated refractive index [3]. If the beam overlap is large enough, significant interaction is obtained by phase matching [2]. This is obtained at a condition called the Bragg condition which relates the angles of incidence and diffraction to the optical and acoustic wavelengths [3]. The diffracted wave is frequency shifted up or down by the acoustic frequency [3]. Acousto-optics has been utilized in devices for manipulation of light beams since the development of lasers in the 1960s [2]. Some examples are acousto-optic modulators and acousto-optic tunable filters [3].

Using the same underlying mechanism as in acousto-optics, interaction between audible sound and radio waves in the MHz-GHz range has been applied to remote sensing under the name Radio Acoustic Sounding System (RASS) [4], [5]. In this application, the acoustic and electromagnetic sources are approximately co-located, transmitting into the air. The diffraction resulting from the Bragg condition is a back scattering of the electromagnetic wave by the acoustic wave [5]. The condition no longer holds if the acoustic wave speed is changed, for example by a change in temperature. This is utilized in RASS to detect temperature profiles in the atmosphere [5]. Other proposed applications for RASS are detection of aircraft wake vortices [6] and early detection of forest fires [7].

Other interaction mechanisms exist. Excitation of acoustic resonances in a radar target result in a Doppler-shifted scattered electromagnetic wave [8], which can be used for land mine detection [9] and non-destructive testing [8]. A similar effect has been proposed for use in breast-cancer imaging [10]. An acoustic wave can cause frequency shift of multiply scattered light, which is used in ultrasound-mediated optical tomography [11].

This work focuses on the interaction mechanism active in acousto-optics and RASS. Ultrasound and mm-waves, where acoustic and electromagnetic wavelengths are similar, are primarily considered. The basic theory of photoelasticity is explored as a physical basis for the coupling between waves. Analytical modeling is used for finding a condition equivalent to the Bragg condition, and order of magnitude estimates for signal-to-noise ratio (SNR). Simulations are presented for confirming the Bragg condition, and as a way of exploring the phenomenon further.

II. ACOUSTIC WAVE PROPAGATION

Acoustic waves can propagate in both fluids and solids, but with different characteristics. In fluids the propagation is purely longitudinal, while in solids both longitudinal and transverse modes exist [12]. The acoustic pressure is described by the wave equation both for linear acoustics in fluids and p-waves in linear elastic solids [12], [13]. The wave speed is $v = \sqrt{K/\rho_0}$ in fluids [12] and $v = \sqrt{(K + 4\mu/3)/\rho_0}$ in solids [12], [13]. K is the bulk modulus, μ the shear modulus and ρ_0 the unperturbed density of the medium.

III. PHOTOELASTICITY

A. Basic Theory

The effect of a mechanical strain s_j on refractive index n_i^2 can be written as [2], [3]

$$\Delta\left(\frac{1}{n_i^2}\right) = p_{ij} s_j \tag{1}$$

where p_{ij} is the photoelastic tensor. Repeated indices imply summation, and tensor indices have been reduced due to tensor symmetry [2], [3]. The equation can be altered to use relative permittivity as $\varepsilon_{\mathrm{r}_i} = n_i^2$. A scalar model is obtained by assuming that the medium is mechanically and electrically isotropic, and that remaining components of p_{ij} are equal [13]. This model can be expressed as [13]

$$\varepsilon_1 = \frac{\varepsilon_r^2 \mathfrak{p}}{K} p \tag{2}$$

where ε_1 is the perturbation in relative permittivity, $\mathfrak{p}$ is the scalar photoelastic constant, K is the bulk modulus and p is the pressure.

One possible relation between $\mathfrak{p}$ and ε_r ($\varepsilon_r \geq 1$) is [2], [13]

$$\mathfrak{p} = \frac{(\varepsilon_\mathrm{r} - 1)(\varepsilon_\mathrm{r} + 2)}{3\varepsilon_\mathrm{r}^2}. \tag{3}$$

This has its origin in the Lorentz-Lorenz relation, implicitly including density. Equation (3) typically only holds for fluids, as more complicated and anisotropic effects have to be considered otherwise [2].

B. Examples of Photoelastic Constant

Equation (3) can be compared with the literature. In [14], the dielectric perturbation in dry air is given by

$$\varepsilon_1 = \frac{1.13 \cdot 10^{-6} p}{T} \tag{4}$$

where p is the pressure in Pa and T the temperature in K. Dry air at 273 K has the properties $\rho_0 = 1.293$ kg/m^3, $v = 331.3$ m/s [12] and $\varepsilon_r = 1.00059$ [15]. This gives a ratio $\varepsilon_1/p = 4.1 \cdot 10^{-9}$ Pa^{-1} using (4). The model presented here instead gives a ratio of $4.2 \cdot 10^{-9}$ Pa^{-1} [13], which is very close to the value from the literature. Additionally, the photoelastic constant in air calculated by (3) is $\mathfrak{p} = 0.00059$.

In [16] the photoelastic constant was measured for 26 liquids. The definition of $\mathfrak{p}$ was slightly different though, requiring multiplication with $2/n^3$ where n is the refractive index [2] (in [2] the factor contains a minus sign, but this is due to a sign difference in definitions). The liquids in [16] had measured values of $\mathfrak{p}$ between water at 0.274 and methylene iodide at 0.332 (values converted as discussed above). [16] also compares measured values with values calculated using the Lorentz-Lorenz relation. Measured values are consistently lower than theoretical due to the Lorentz-Lorenz relation being inaccurate for liquids [16].

Measured values of photoelastic tensor components are now presented for completeness. Fused quartz has the components $p_{11} = +0.121$, $p_{12} = +0.270$, $p_{44} = -0.075$ [17]. Diamond has the components $p_{11} = -0.244$, $p_{12} = +0.042$, $p_{44} = -0.172$ [18]. The three components presented are sufficient for describing the full tensor using isotropic or cubic crystal symmetry [3].

IV. ELECTROMAGNETIC MODELING

The model presented in this section is described in more detail in [13] where full derivations are available. The approach is similar to that in [19].

A. Basic Model

The permittivity of the perturbed medium is defined as

$$\varepsilon = \varepsilon_0(\varepsilon_\mathrm{r} + \varepsilon_1) \tag{5}$$

where ε_0 is the permittivity of free space, ε_r is the unperturbed relative permittivity (frequency independent) and ε_1 is the perturbation in relative permittivity. It is assumed that $|\varepsilon_1| \ll \varepsilon_\mathrm{r}$. An electric field is split into the incident part $\boldsymbol{E}_\mathrm{i}$ and the part scattered by the dielectric perturbation $\boldsymbol{E}_\mathrm{sc}$. If the scattered field is small compared to the incident field (Born approximation), the scattering is described by [13]

$$\begin{aligned}\nabla^2 \boldsymbol{E}_\mathrm{sc}(\boldsymbol{r},t) + k^2 \boldsymbol{E}_\mathrm{sc}(\boldsymbol{r},t) &= -k^2 \frac{\varepsilon_1(\boldsymbol{r},t)}{\varepsilon_\mathrm{r}} \boldsymbol{E}_\mathrm{i}(\boldsymbol{r}) \\ &- \frac{1}{\varepsilon_\mathrm{r}} \nabla(\boldsymbol{E}_\mathrm{i}(\boldsymbol{r}) \cdot \nabla \varepsilon_1(\boldsymbol{r},t)) - \frac{k^2}{\varepsilon_\mathrm{r}} \boldsymbol{E}_\mathrm{di}(\boldsymbol{r},t)\end{aligned} \tag{6}$$

which is an inhomogeneous Helmholtz equation where k is the wavenumber. All electric fields are complex amplitudes with a $-\mathrm{i}\omega t$ time-dependence separated. However, a weaker time-dependence remains in the scattered field due to the time-varying dielectric perturbation. The remaining time derivatives are collected in

$$\boldsymbol{E}_\mathrm{di}(\boldsymbol{r},t) = \frac{2\mathrm{i}\boldsymbol{E}_\mathrm{i}(\boldsymbol{r})}{\omega} \frac{\partial}{\partial t} (\varepsilon_1(\boldsymbol{r},t)) - \frac{\boldsymbol{E}_\mathrm{i}(\boldsymbol{r})}{\omega^2} \frac{\partial^2}{\partial t^2} (\varepsilon_1(\boldsymbol{r},t)) \tag{7}$$

where ω is the electromagnetic angular frequency. In three dimensions, the solution for the scattered field is given by the integral

$$\begin{aligned}\boldsymbol{E}_\mathrm{sc}(\boldsymbol{r},t) = \frac{1}{4\pi\varepsilon_\mathrm{r}} \int_V \frac{\mathrm{e}^{\mathrm{i}k|\boldsymbol{r}-\boldsymbol{r}'|}}{|\boldsymbol{r}-\boldsymbol{r}'|} \big(k^2 \varepsilon_1(\boldsymbol{r}',t) \boldsymbol{E}_\mathrm{i}(\boldsymbol{r}') \\ + \nabla\left(\boldsymbol{E}_\mathrm{i}(\boldsymbol{r}') \cdot \nabla \varepsilon_1(\boldsymbol{r}',t)\right) + k^2 \boldsymbol{E}_\mathrm{di}(\boldsymbol{r}',t)\big) \mathrm{d}v'\end{aligned} \tag{8}$$

where V is the volume where both $\boldsymbol{E}_\mathrm{i}$ and ε_1 are nonzero.

B. Calculation Using Simplified Fields

For a simple analytical calculation, $\boldsymbol{E}_\mathrm{i}$ and ε_1 are modeled as plane waves within specified beam regions and zero outside. The overlap between the electric and acoustic beam regions defines a region where both $\boldsymbol{E}_\mathrm{i}$ and ε_1 are nonzero. This is referred to as the interaction region, and there the following holds for the electric field

$$\boldsymbol{E}_\mathrm{i}(\boldsymbol{r}') = \boldsymbol{E}_\mathrm{i0} \mathrm{e}^{\mathrm{i}\boldsymbol{k} \cdot \boldsymbol{r}'} \tag{9}$$

where $\boldsymbol{E}_\mathrm{i0}$ is the amplitude of the incident field and $\boldsymbol{k}$ is the electromagnetic wavevector. The dielectric perturbation is

$$\varepsilon_1(\boldsymbol{r}',t) = \frac{\varepsilon_\mathrm{r}^2 \mathfrak{p}}{K} p_0 \cos(\boldsymbol{q} \cdot \boldsymbol{r}' - \Omega t) \tag{10}$$

where p_0 is the unperturbed pressure, $\boldsymbol{q}$ is the acoustic wavevector and Ω is the acoustic angular frequency. Fig. 1 shows the geometry of the problem. The electromagnetic beam width is d_e and the acoustic beam width is d_a. Both beams are assumed to have rectangular cross-sections, extending L_z in z. The observation point $\boldsymbol{r}$ is at a distance r from the center of the interaction region at azimuthal angle ϕ and polar angle θ (not shown).

The incident electric field is polarized in z, and the incident acoustic wave propagates in the xy-plane. $\boldsymbol{E}_\mathrm{sc}$ is assumed to be in the far-field, simplifying the Green function. It is further assumed that $\Omega \ll \omega$, which is true for mm-waves and ultrasound.

Under these conditions, the scattered field is [13]

$$\boldsymbol{E}_\mathrm{sc}(\boldsymbol{r},t) = \boldsymbol{E}_\mathrm{i0} \left(E_\mathrm{A}^+(\boldsymbol{r},t) + E_\mathrm{A}^-(\boldsymbol{r},t)\right) \tag{11}$$

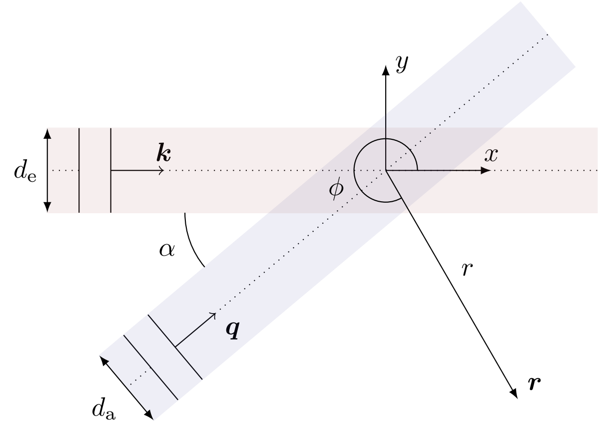

Fig. 1. Geometry used in analytical calculations.

where

$$E_\mathrm{A}^{\pm}(\boldsymbol{r},t)=\frac{\varepsilon_\mathrm{r}k^2\mathrm{e}^{\mathrm{i}kr}\mathfrak{p}p_0}{8\pi rK}\frac{d_\mathrm{a}d_\mathrm{e}L_z}{\sin\alpha}e^{\mp\mathrm{i}\Omega t}\Phi^{\pm} \tag{12}$$

and

$$\begin{aligned}\Phi^{\pm}=&\mathrm{sinc}\left(\frac{d_\mathrm{a}}{2\pi\sin\alpha}(k-k\sin\theta\cos\phi\pm q\cos\alpha)\right)\\ \cdot&\mathrm{sinc}\left(\frac{d_\mathrm{e}}{2\pi\tan\alpha}(k-k\sin\theta(\cos\phi+\sin\phi\tan\alpha)\right.\\ &\qquad\left.\pm q(\cos\alpha+\sin\alpha\tan\alpha))\right)\\ \cdot&\mathrm{sinc}\left(-\frac{L_z}{2\pi}k\cos\theta\right)\end{aligned} \tag{13}$$

The factor $\mathrm{e}^{\mp\mathrm{i}\Omega t}$ in (12) indicates a frequency shift of $\pm\Omega$ for $E_\mathrm{A}^{\pm}(\boldsymbol{r},t)$. Thus $\boldsymbol{E}_\mathrm{sc}(\boldsymbol{r},t)$ has two frequency components - one at frequency $\omega+\Omega$ and one at $\omega-\Omega$. However, $\Phi^{\pm}$ limits the angles where strong interaction is possible. If (13) is analyzed, a maximizing condition is found when all sinc functions are zero. The condition for incident waves is [13]

$$\cos\alpha=\mp\frac{q}{2k}=\mp\frac{\lambda}{2\Lambda} \tag{14}$$

where λ is the electromagnetic wavelength and Λ the acoustic wavelength. The observation point should be in the same plane as the incident waves, as well as at the azimuth angle $\phi=\mp\pi+2\alpha$ [13].

The maximum of $\Phi^{\pm}$ almost gives the conditions for maximum scattering, but the factor $1/\sin\alpha$ in (12) complicates matters. This factor contains the effect of the interaction region increasing as α decreases. The effect of this is maximum scattering at a different α than given by (14) [13]. However, this is not explore further as such details are outside the scope of this rough modeling.

C. Radar Equation

Using more system parameters, a radar equation for SNR can be written as

$$SNR_N^{\pm}=\frac{P_\mathrm{T}G_\mathrm{T}G_\mathrm{R}\lambda_\mathrm{R}^2\sigma^{\pm}(\theta,\phi)}{(4\pi)^3R_\mathrm{T}^2R_\mathrm{R}^2k_\mathrm{B}T_0BF}N \tag{15}$$

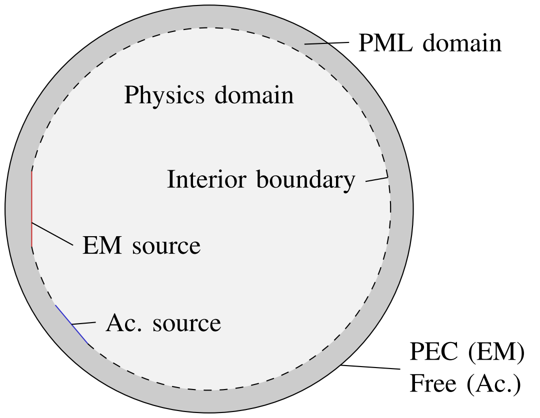

Fig. 2. Simulation geometry for both the acoustic (Ac.) and electromagnetic (EM) problem.

where P_T is the power accepted by the transmitting antenna, G_T is the gain of the transmitting antenna, G_R is the gain of the receiving antenna, λ_R is the wavelength at the receiving antenna, R_T is the range from the transmitting antenna to the interaction region center, R_R is the range from the interaction region center to the receiving antenna, k_B is Boltzmann's constant, T_0 is the standard temperature for noise, B is the receiver bandwidth, F is the noise ratio of the receiver and N is the number of samples recorded. Coherent demodulation and integration of the signal is assumed [13].

The equation is a bistatic radar equation with an equivalent radar cross-section (RCS) given by

$$\sigma^{\pm}(\theta,\phi)=\frac{\varepsilon_\mathrm{r}^2k^4\mathfrak{p}^2p_0^2}{16\pi K^2}\frac{d_\mathrm{a}^2d_\mathrm{e}^2L_z^2}{\sin^2\alpha}\Phi^{\pm}(\theta,\phi)^2 \tag{16}$$

This parameter contains all connection to the acousto-electromagnetic problem. It should be noted that the radar equation is based on a very rough model, but may still be able to provide order of magnitude estimates for SNR [13].

V. SIMULATION SETUP

A. General Details

To verify and expand on the results of the analytical model, simulations were conducted in COMSOL Multiphysics. Both acoustic and electromagnetic simulations were 2D frequency domain, but for different frequencies. One effect of this setup was the inability to simulate frequency shifts in the electromagnetic wave. The simulation geometry is shown in Fig. 2. To simulate an open boundary, a perfectly matched layer (PML) was used outside of the physics domain for both simulations. Its typical wavelength was the maximum of λ and Λ. The mesh for both simulations was based on an edge mesh on the interior boundary. From this, a free triangular mesh in the physics domain and a mapped quadrilateral mesh in the PML domain were generated. The maximum element size was 1/10 of the smallest wavelength. The material simulated was based on the properties of polystyrene in [20] with parameter values within the listed ranges.

B. Acoustic Simulation

Acoustic waves were simulated using solid mechanics for correct handling of p-waves in solids. The source was modeled using a prescribed displacement boundary condition on a boundary segment with length 8Λ. The displacement amplitude was set to 5 nm and a Gaussian taper was applied to decrease sidelobe levels. The acoustic frequency was set to 1 MHz. A free boundary condition was used at the end of the PML domain. The solid was modeled as an isotropic solid and plane strain conditions were used. The material had a Young's modulus $E = 1.8$ GPa, Poisson's ratio $\nu = 0.22$ and density $\rho_0 = 600$ kg/m^3.

C. Photoelastic Coupling

The photoelastic model used was the simple scalar model in (2). For simplicity, (3) was used to model the photoelastic constant even though the material was a solid. The relative permittivity used was $\varepsilon_r = 2.4$, and the material was nonmagnetic and nonconducting. The bulk modulus K was calculated automatically from E, ν and ρ_0. The real part of the pressure from the acoustic simulation was used in (2) to calculate ε_1 in the physics domain.

D. Electromagnetic Simulation

Two electromagnetic simulations were performed where photoelasticity was either enabled or disabled. The photoelastically scattered electric field was calculated as the difference between the two fields. The electromagnetic source was modeled using a port boundary condition on a boundary segment with length 8λ. The port input power was set to 15 dBm with the electric field polarized in z and the propagation constant equal to the wavenumber in the medium. As in the acoustic case, a Gaussian taper was applied to the field. The electromagnetic frequency was matched to the acoustic frequency using the condition in (14) with $\alpha = 40°$, resulting in a frequency of 68 GHz. A perfect electric conductor (PEC) boundary condition was used at the end of the PML domain.

E. Post-processing

The photoelastically scattered electric and magnetic fields resulting from simulations were evaluated at the interior boundary (see Fig. 2). In post-processing the time-averaged Poynting vector was calculated along the boundary. The total photoelastically scattered power was then calculated by integrating the normal component of the time-averaged Poynting vector along the full interior boundary. The trapezoidal rule was used with interval lengths extracted from the geometry data.

F. Simulation Cases

Two different simulation cases are presented in this work. The first is a sweep of the angle α with the wavelengths matched to $\alpha = 40°$ as described earlier. The purpose of this was to show how the scattering is affected by altering the angle between incident waves. The second is a sweep of the density ρ_0 in a small inclusion of the interaction region.

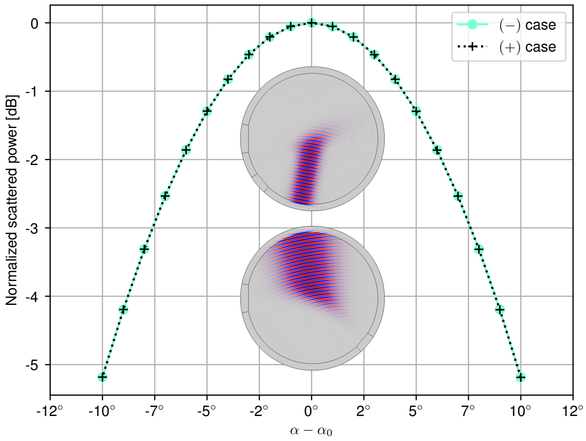

Fig. 3. Total photoelastically scattered power for angle sweep. Normalized to peak value for $(-)$ case: -68.24 dBm. Sweep midpoints $\alpha_0 = 40°$ $(-)$ and $\alpha_0 = 140°$ $(+)$. Insets show scattered electric field for $\alpha = 40°$ $(-)$ (top) and $\alpha_0 = 140°$ $(+)$ (bottom).

VI. SIMULATION RESULTS

A. Angle Sweep

The electromagnetic and acoustic wavelengths were matched according to (14) for $\alpha = 40°$. This is for the $(-)$ case. The $(+)$ case for those wavelengths instead results in $\alpha = 140°$ being the matched angle. Simulations were conducted for both $\alpha = 40° \pm 10°$ and $\alpha = 140° \pm 10°$. The total photoelastically scattered power for different α is shown in Fig 3 for both cases. From Fig 3 it is clear that the condition in (14) holds well for both the $(-)$ and $(+)$ cases. The total scattered power is the same for both cases, but it should be noted that the scattered power density is greater in the $(-)$ case. The maximum of the power density at $40°$ in the $(-)$ case was 14.2 nW/m^2, while it was 5.12 nW/m^2 at $140°$ in the $(+)$ case. This is due to the wider beam in the $(+)$ case, as can be seen qualitatively in the insets of Fig 3.

Earlier it was discussed that the factor $1/\sin\alpha$ in (12) would result in a shifted α for the maximum. This is not observed in the simulation results. The shift might be too minor to be detected, or may simply be an artifact of the rough model used.

B. Density Sweep

In this simulation case, the angle α was fixed at $40°$ with the wavelengths matched as before. The density was varied inside of an inclusion of the interaction region with the diameter λ. The total photoelastically scattered power for different density is shown in Fig 4. It is clear from Fig 4 that a change in the density affects the interaction. The main mechanism at work here is the diffraction of the acoustic wave by the inclusion. This introduces nulls in the acoustic field and changes the propagation direction for parts of the wave. This can be seen qualitatively in the inset of Fig 4. Close to nulls, lower acoustic pressure weakens interaction. Where the propagation direction

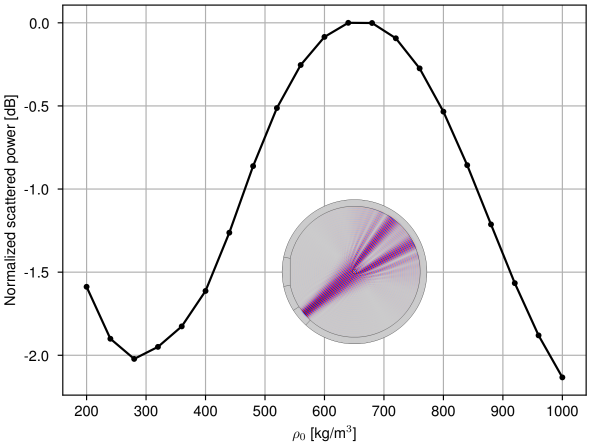

Fig. 4. Total photoelastically scattered power for density sweep. Normalized to peak value: -68.15 dBm. Inset shows acoustic pressure for the inclusion density $\rho_0 = 360$ kg/m^3.

is changed, the Bragg condition no longer holds, which also weakens interaction.

The scattered power might be expected to decrease as the density moves away from 600 kg/m^3. However, the peak in Fig. 4 is at $\rho_0 > 600$ kg/m^3. The reason for this is that the inclusion acts as an acoustic lens if the density is higher than its surroundings, increasing power slightly [13]. Another interesting detail is the shift in the slope at $\rho_0 < 300$ kg/m^3. This might be due to an increase in the forward-scattered component of the acoustic wave, as the Bragg condition holds for that part of the wave. Effects similar to this were seen if the conductivity was varied, with the electromagnetic wave being scattered by the inclusion instead [13].

VII. CONCLUSION

A model for acousto-electromagnetic interaction based on photoelasticity was presented. The conditions for strong interaction corresponded well to the Bragg condition in acousto-optics. A radar equation for estimating the SNR was presented. Although based on a rough model, it could be useful for order of magnitude estimations in a measurement situation.

Multiphysics simulations with a simple photoelastic relation connecting acoustic pressure and relative permittivity confirmed the Bragg condition for strong scattering. Simulations also allowed for the study of beam widths for the photoelastically scattered wave. This is not possible from the Bragg condition alone. Further simulation showed how a small inclusion with material contrast impacted the interaction. Effects similar to this are widely studied in the literature, for example in the context of RASS. The shorter wavelengths of ultrasound and mm-waves combined with the increased photoelasticity of solids might present a new possibility for applications in, for example non-destructive testing.

ACKNOWLEDGMENT

This work was supported in part by the Swedish Armed Forces, in part by the Swedish Defence Materiel Administration, in part by the National Aeronautics Research Program and in part by the Swedish Governmental Agency for Innovation Systems.

REFERENCES

[1] L. Brillouin, “Diffusion de la lumière et des rayons x par un corps transparent homogène - influence de l’agitation thermique,” *Ann. Phys.*, vol. 9, no. 17, pp. 88–122, 1922.

[2] A. Korpel, *Acousto-optics*, 1st ed., ser. Optical engineering, 16. New York: Marcel Dekker Inc, 1988.

[3] B. E. A. Saleh and M. C. Teich, *Acousto-Optics*, 2nd ed., ser. Fundamentals of Photonics. Hoboken, New Jersey: John Wiley & Sons, Inc., 2007, ch. 19, pp. 804–833.

[4] J. M. Marshall, A. M. Peterson, and A. A. Barnes, “Combined radar-acoustic sounding system,” *Applied Optics*, vol. 11, no. 1, pp. 108–112, Jan 1972.

[5] N. Matuura, Y. Masuda, H. Inuki, S. Kato, S. Fukao, T. Sato, and T. Tsuda, “Radio acoustic measurement of temperature profile in the troposphere and stratosphere,” *Nature*, vol. 323, no. 6087, p. 426, Oct. 1986.

[6] W. L. Rubin, “Radar–acoustic detection of aircraft wake vortices,” *Journal of Atmospheric and Oceanic Technology*, vol. 17, no. 8, pp. 1058–1065, 2000.

[7] Y. G. Sahin and T. Ince, “Early forest fire detection using radio-acoustic sounding system,” *Sensors*, vol. 9, no. 3, pp. 1485–1498, 2009.

[8] A. Buerkle and K. Sarabandi, “Non-destructive evaluation of elastic targets using acousto-electromagnetic wave interaction and time reversal focusing,” *IEEE Transactions on Antennas and Propagation*, vol. 57, no. 11, pp. 3628–3637, Nov. 2009.

[9] W. R. Scott and J. S. Martin, “Experimental investigation of the acousto-electromagnetic sensor for locating land mines,” *Proc.SPIE*, vol. 3710, pp. 204 – 214, 1999.

[10] A. K. Tafreshi, C. B. Top, and N. G. Gençer, “Two-dimensional multi-frequency imaging of a tumor inclusion in a homogeneous breast phantom using the harmonic motion doppler imaging method,” *Physics in Medicine & Biology*, vol. 62, no. 12, p. 4852, 2017.

[11] D. S. Elson, R. Li, C. Dunsby, R. Eckersley, and M.-X. Tang, “Ultrasound-mediated optical tomography: a review of current methods,” *Interface Focus*, vol. 1, no. 4, pp. 632–648, 2011.

[12] T. Rossing, Ed., *Springer Handbook of Acoustics*, 2nd ed. Springer-Verlag, 2014.

[13] N. Wingren, “Acousto-electromagnetic interaction in materials for aerospace composites,” M.S. Thesis, Dept. of Elect. and Inform. Technol., Lund Univ., Lund, Sweden, 2019.

[14] V. O. Rapoport, N. A. Mityakov, V. A. Zinichev, and N. I. Belova, “The role of atmospheric temperature gradients and winds for estimating the energy potential of radio-acoustic sounding systems,” *Radiophysics and Quantum Electronics*, vol. 40, no. 5, pp. 408–413, May 1997.

[15] L. G. Hector and H. L. Schultz, “The dielectric constant of air at radiofrequencies,” *Physics*, vol. 7, no. 4, pp. 133–136, 1936.

[16] N. Uchida, “Elastooptic coefficient of liquids determined by ultrasonic light diffraction method,” *Japanese Journal of Applied Physics*, vol. 7, no. 10, pp. 1259–1266, oct 1968.

[17] R. W. Dixon, “Photoelastic properties of selected materials and their relevance for applications to acoustic light modulators and scanners,” *Journal of Applied Physics*, vol. 38, no. 13, pp. 5149–5153, 1967.

[18] O. Madelung, U. Rössler, and M. Schulz, Eds., *Group IV Elements, IV-IV and III-V Compounds. Part b - Electronic, Transport, Optical and Other Properties*, ser. Landolt-Börnstein - Group III Condensed Matter. Springer-Verlag Berlin Heidelberg, 2002, vol. 41A1β, ch. Diamond (C), elastooptic constants, further optical properties.

[19] V. I. Tatarskii, *The effects of the turbulent atmosphere on wave propagation.* Jerusalem: Israel Program for Scientific Translations, 1971. [Online]. Available: https://ui.adsabs.harvard.edu/#abs/1971etaw.book.....T

[20] MatWeb, “Overview of materials for polystyrene, molded, unreinforced.” [Online]. Available: http://www.matweb.com/search/DataSheet.aspx?MatGUID=df6b1ef50ce84e7995bdd1f6fd1b04c9